



A detailed study of Au–Ni bimetal synthesized by the phase separation mechanism for the cathode of low-temperature solid oxide fuel cells



Tao Yang*, Carlos Manuel Rodrigues de Almeida, Devaraj Ramasamy, Francisco José Almeida Loureiro

TEMA-NRD, Mechanical Engineering Department, Aveiro Institute of Nanotechnology (AIN), University of Aveiro, 3810-193 Aveiro, Portugal

HIGHLIGHTS

- Phase separation mechanism was utilized to save 25% of the noble metal Au.
- A highly active property towards oxygen reduction reactions was achieved.
- Size effect and surface energies differences were used to get nanosphere AuNi.
- A delicate cut and elemental mapping confirmed the core–shell structure of AuNi.
- Morphological and compositional aspects of catalysts were thoroughly investigated.

ARTICLE INFO

Article history:

Received 2 June 2014

Received in revised form

25 June 2014

Accepted 27 June 2014

Available online 7 July 2014

Keywords:

Au–Ni

Phase separation

Nanosphere

XPS

Cathode and SOFCs

ABSTRACT

A facile co-reduction and annealing synthesis route of nanospheric particles of Au–Ni bimetal with adjustable composition was developed. In a typical synthesis, a direct co-reduction of $\text{HAuCl}_4 \cdot 4\text{H}_2\text{O}$ and NiCl_2 in aqueous solution was performed with the assistance of reductive NaBH_4 and an anionic surfactant sodium dodecyl sulfate (SDS) functioned as the structure-directing agent. Ultrasonic mixing was used at the same time to control the size of the particles. The morphology, microstructure and the state of the surface atoms were analyzed in detail. These nanospheres showed enhanced electrocatalytic activity towards oxygen reduction reaction than that of pure Au nanoparticles, demonstrated in the low temperature SOFC as cathode. The maximum power density generated is 810 mW cm^{-2} at 550°C . This is a promising route of taking advantages the Phase Separation Mechanism to greatly reduce the use of noble metals in the ORR field without sacrificing the electrocatalytic activity.

© 2014 Elsevier B.V. All rights reserved.

1. Introduction

Solid oxide fuel cells (SOFCs) are one of the favorite power sources amongst various fuel cells due to the diversity of useable fuels such as H_2 , formic acid, methanol, ethanol, propyl alcohol, glucose and various hydrocarbons. However, the cost of rare metals or ceramic support, catalyst and the maintenance in high temperature have seriously handicapped their commercialized development. For decades, great efforts have been devoted to lowering the temperature of SOFCs to $550\text{--}800^\circ\text{C}$, [1–5] where the choice of materials can be expanded and the reliability of cell components

will also be improved. In order to reduce the operational temperature without hampering/decreasing the power density, efficient catalysts must be used. Noble metals such as Au, Pd and Pt are the ideal option when only the catalytic activity is taken into account, but the cost is high. There are two ways to deal with this issue.

The first one is to partially replace the noble metal in the catalysts, such as intermetallic compounds, metallic sulfides, metallic oxides, metallic carbides and organometallic compounds; [6–10] The effect of non-noble metal Co, Ni, Bi underlayers/surface impurities on the properties of noble metal overlayers has been successfully utilized towards oxygen reduction for a number of bimetallic systems in the authors former research [11–13]. As is known, nickel represents a unique electrode metal (anodic and cathodic material) of extremely importance for experimental studies and practical industrial applications.

* Corresponding author. Tel.: +351 916969863; fax: +351 234 370 953.
E-mail addresses: yangtao@ua.pt, 21825550@qq.com (T. Yang).

Nickel is located above the noble metals of Pd and Pt in group VIII of the periodic table and therefore in general behaves similarly to them, and shows similar electrochemical properties. Also, nickel, as a non-noble transition element and due to its availability, plays the role of noble metals for both anodic and cathodic processes in many electrochemical environments. And due to the pronounced passivation features, it shows much higher stability than Co and Fe. It does not rust or suffer from the problems caused by rust.

The second one is to use less amount of noble metal by taking advantage of highly functional nanoparticles. Certain nanoscale morphologies and microstructures are often associated with a perturbation of the outmost layer geometry on an atomic scale [14,15].

In the previous work, the author has tried to improve the properties of the cathode in SOFCs by coating Au nanoparticles onto BICUVOX10($\text{Bi}_2\text{Cu}_{0.1}\text{V}_{0.9}\text{O}_{5.35}$), [16] based on previous findings that Au nanoparticles on appropriate carriers can reduce oxygen at low temperatures [17–19]. The Au nanoparticles not only functioned as an electronic network, but also decreased the polarization of the cathodic oxygen reduction reaction. So, in this work, those two ways were combined and Au–Ni binary immiscible systems were prepared with highly organized spherical morphology. The epitaxial constraints stabilizing a homogeneous solid solution on the particles' surface against a phase separation lateral or transverse inhomogeneities were focused in this research. The catalytic activity of the synthesized nanoparticles towards oxygen reduction as the SOFCs cathode was also examined.

2. Experimental section

2.1. Synthesis of the AuNi powders

The chemicals $\text{HAuCl}_4 \cdot 4\text{H}_2\text{O}$, NiCl_2 , SDS, HCl and NaBH_4 used are all from Alfa Aesar, with purity above 99.9%. In a typical synthesis, 0.1 g of $\text{HAuCl}_4 \cdot 4\text{H}_2\text{O}$, 0.02 g of NiCl_2 , 0.25 g of SDS was dissolved in 250 mL of deionized water to form a golden aqueous solution. The pH of the reacting solution was tuned to 4 by HCl addition and then the flask containing the solution was maintained in the bath-type ultrasonicator with a frequency of 100 kHz and temperature of 80 °C. 100 mL of 0.05 M NaBH_4 fresh solution was added drop-wise into the flask afterwards. While the reaction took place, the golden solution turned to a bright tartaric color and quickly a black precipitate was obtained on the bottom of the flask. After filtered and washed with deionized water, the powder was dried in an oven at

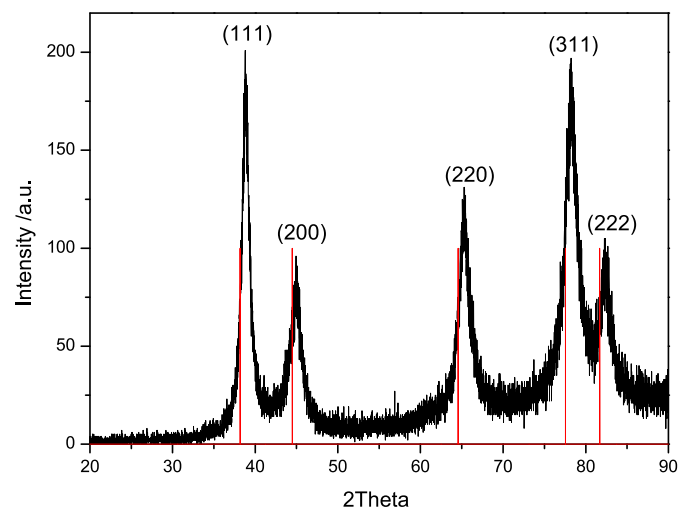


Fig. 1. XRD patterns of $\text{Au}_{90}\text{Ni}_{10}$.

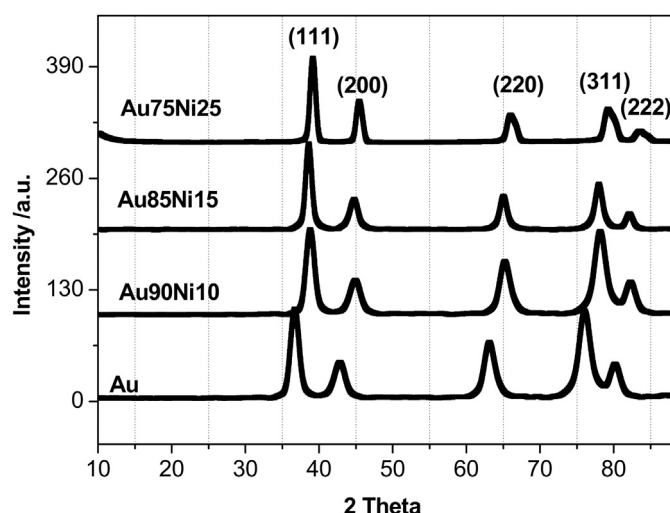


Fig. 2. XRD patterns of Au, $\text{Au}_{90}\text{Ni}_{10}$, $\text{Au}_{85}\text{Ni}_{15}$ and $\text{Au}_{75}\text{Ni}_{25}$.

50 °C. Then the powder was heat-treated at 750 °C in a H_2 -Ar atmosphere (H_2 vol. 5%) for 2 h with the increasing temperature rate of 10 °C min^{-1} and decreasing temperature rate of 50 °C min^{-1} . After cooled to room temperature, the powder was washed with 2 M HCl solution and deionized water each for three times and dried in the oven at 50 °C.

2.2. Characterization

The samples were characterized by X-ray diffraction by a German Bruker D-8 Advance Diffract Meter with $\text{Cu K}\alpha$ ($\lambda = 1.5405$ Å) radiation. The patterns were recorded between 10 and 80° at increments of 0.02° and counting time of 2s per step. The morphology of the samples was observed in a Jeol JSM-6500F SEM with EDX. The microstructure of the samples was investigated by a Jeol MCL J-2010 Transmission Electron Microscope (TEM) with an accelerating voltage of 200 kV. Before the TEM experiments were performed, the samples were prepared by dispersing a suspension of particles/isopropyl alcohol onto a 3 mm-diameter copper grid

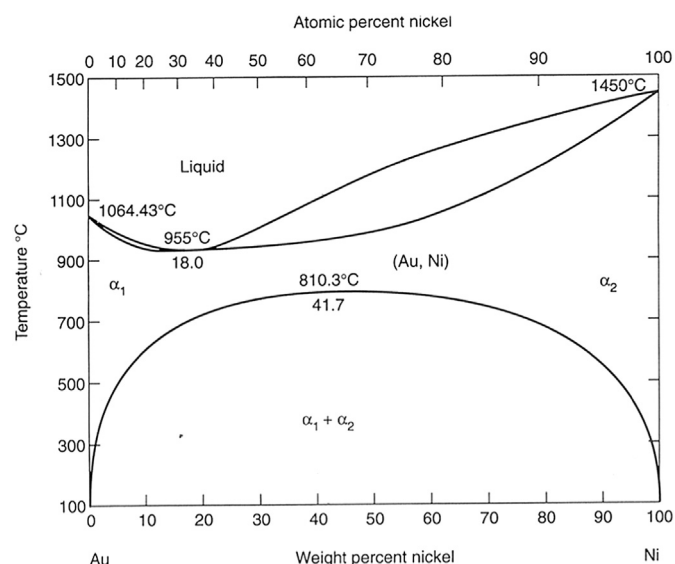


Fig. 3. Phase diagram of Au–Ni.

substrate covered with holey carbon film. The composition of the samples was analyzed by ICP-AES method on an IRIS Intrepid spectrometer after dissolution in aqua regia and diluted with 1 M HCl.

The measurements of XPS were carried out with an X-ray photoelectron spectrometer (Physical Electronics PHI Quantera SXM) using an Al K α monochromatic source ($h\nu = 1486.6$ eV). All the binding energies were corrected by the principal peak's signal of the carbonaceous matrix using 284.8 eV as an internal

standard. After that, the spectra were analyzed using XPSPEAK 4.1 software.

Electrochemical performances (IM6e, Zahner) of the single fuel cell were characterized from 450 to 550 °C with wet hydrogen (vol.2% H₂O) as fuel and O₂ as oxidant at a flow rate of 50 mL min⁻¹. The current–voltage curves were obtained in galvanostat mode and electrochemical impedance spectra were measured under open-circuit conditions in the frequency range from 0.1 Hz to 1 MHz.

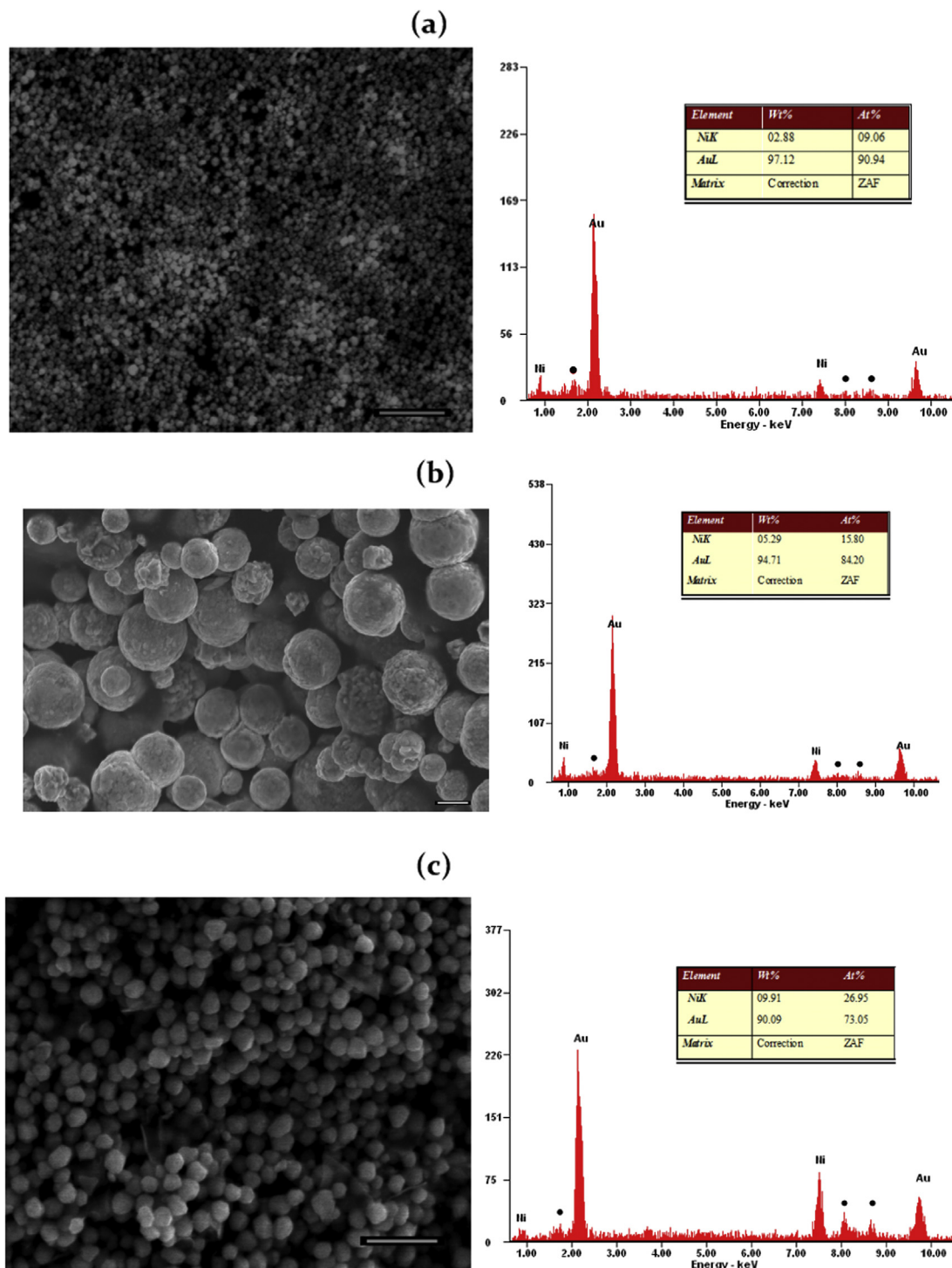


Fig. 4. FE-SEM patterns and EDX analysis of Au–Ni. (a) Au₉₀Ni₁₀. (b) Au₈₅Ni₁₅. (c) Au₇₅Ni₂₅. The bar is 10 μ m in (a), 100 nm in (b) and 1 μ m in (c).

2.3. Fabrication of the cells

The cells were fabricated by the anode-support method. NiO/GDC ($\text{Ce}_{0.9}\text{Gd}_{0.1}\text{O}_{1.95}$ with 60 wt% NiO) powder was pressed uniaxially into small round pieces of diameter 1.0 cm and the GDC electrolyte powder was dry-pressed onto the anode at the same time. The pressed electrolyte was then fired at 1550 °C for 5 h. The Au–Ni powder was brush-painted in the center and fired at 750 °C for 2 h on the half-cells. The diameter of the cathode was 0.5 cm.

3. Results and discussion

3.1. Characterization of the Au–Ni particles

Fig. 1 shows the XRD patterns of the $\text{Au}_{90}\text{Ni}_{10}$ sample. All the diffraction peaks can be assigned to face-centered cubic (FCC) crystalline Au structure with no other peaks detected, suggesting the AuNi did not contain nickel oxides/hydroxides and its other compounds. However, the (111), (200), (220), (311) and (222) crystal planes diffraction all shifted slightly towards higher diffraction angles (the red lines in the XRD patterns are the standard XRD position from Au, JCPDS 00-001-1172). The d value of the Au (111) plane calculated from the Bragg equation $n\lambda = 2d\sin\theta$ is 0.232 nm, 0.004 nm smaller than the standard Au (111) d value 0.236 nm. The standard d value of Ni (111) is 0.204 nm. The shrinkage of the crystal lattice showed that when Ni atoms replaced some Au atoms in the Au structure, it shortened the distance between the atoms.

It was also observed that with the increase of Ni proportion in the particles, the diffraction angles of these nanoparticles shifted to much higher positions, reflecting the increase of Ni in the Au

matrix, the shrinkage of lattice increased, indicating there were more defects in the surface of Au. The smoothed XRD patterns in Fig. 2 revealed there were no diffraction peaks for Ni or its oxides, etc. The higher the substitution of Au by Ni is, the smaller the Au lattice becomes due to the smaller Ni radius. The contraction of the Au lattice structure, namely the epitaxial constraints on the particles' surface against a phase separation lateral or transverse inhomogeneities will benefit the catalytic activity for the Oxygen Reduction Reaction (ORR) in the cathode, attributing to synergism, modification of electronic properties and geometric effects. The bulk composition was calculated from ICP-AES, respectively.

From the phase diagram of Au–Ni (Fig. 3) it can be seen that at higher temperatures Au and Ni form a continuous solid solution. Nonetheless, the miscibility gap at lower temperatures leads to the decomposition of the single-phase bimetal into two face-centred cubic solid solutions. However, in every attempt to synthesize $\text{Au}_{70}\text{Ni}_{30}$ there were always Ni, $\text{Ni}(\text{OH})_2$, Ni_2O_3 and NiO impurities detected using XRD, being Ni the main impurity. The maximum amount of Ni in the Au structure is 75% during the co-reduction and annealing process by reductive reagent NaBH_4 with SDS as the soft template.

3.2. FE-SEM patterns and EDX analysis of Au–Ni

The SEM characterization showed that the black powder was made up of nanospheres, no matter what the ratio of Au vs. Ni was, the morphology was in unity, with average diameter of 50–100 nm (Fig. 4). A closer look to the nanospheres in Fig. 4b, we could see the bigger spheres were made of smaller spheres or nano-sized clumps. The EDX data were presented aside the SEM accordingly. The respective atomic ratios were 90.94:9.06, 84.20:15.8, and

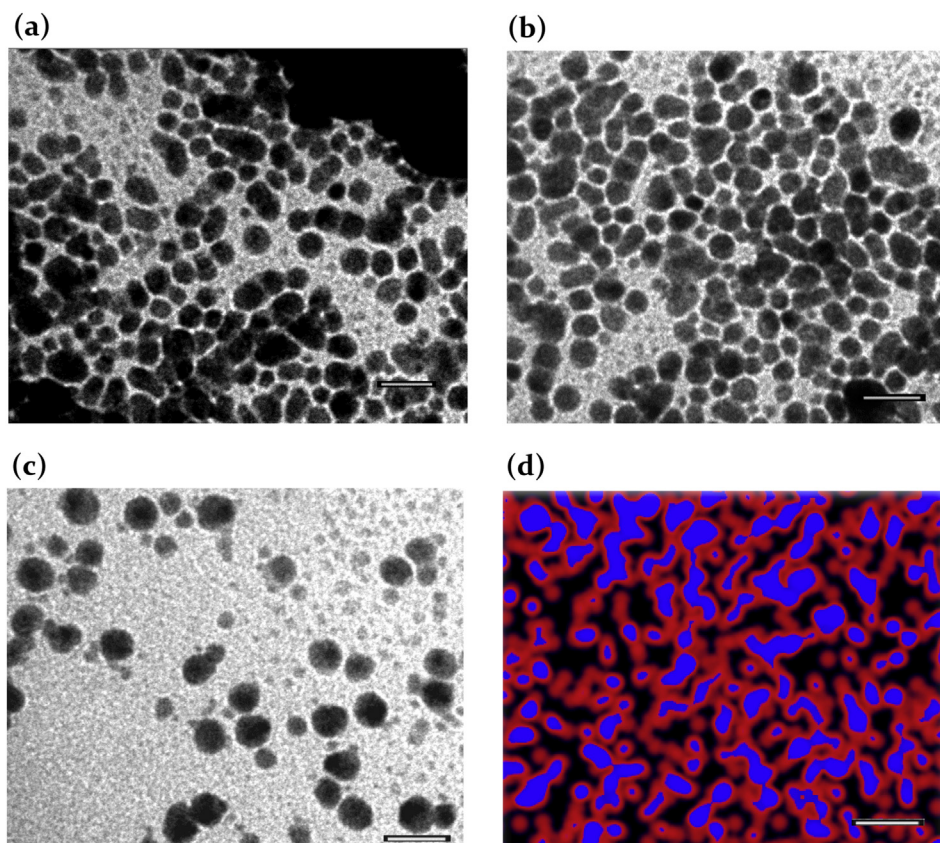


Fig. 5. TEM images and mapping of Au–Ni. (a) $\text{Au}_{90}\text{Ni}_{10}$. (b) $\text{Au}_{85}\text{Ni}_{15}$. (c) $\text{Au}_{75}\text{Ni}_{25}$. and (d) mapping of $\text{Au}_{85}\text{Ni}_{15}$. The bar is 50 nm in (a), (b) (c) and (d).

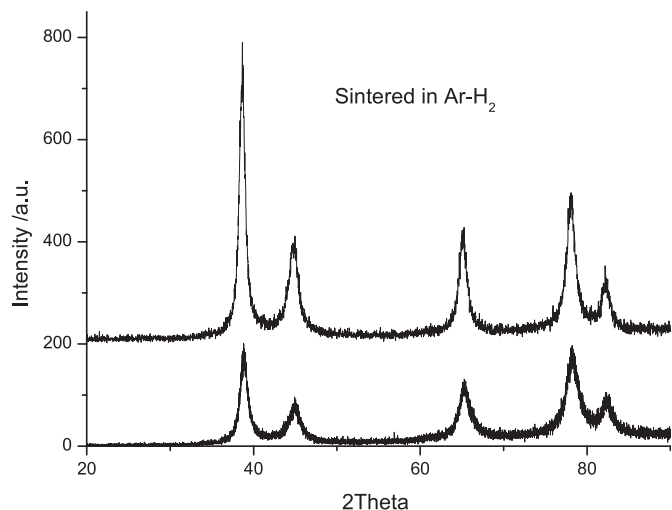


Fig. 6. The XRD patterns of AuNi after sintered in Ar-H₂ for 72 h.

73.05:26.95. The micro area compositions of Au:Ni were in agreement with the bulk composition calculated from ICP-AES, which was 90:10, 85:15, and 75:25. The peaks indexed by black dots in the EDX spectra came from the contribution of the copper sample holder. There were no other species detected in the EDX, either.

3.3. TEM patterns of Au–Ni

TEM characterization confirmed that the particles were spherical with diameters ranging from 10 to 100 nm. In Fig. 5a, with Au₉₀Ni₁₀, there were more dark spheres because the Au percentage was relatively higher. The huge chunk in the corner was due to inadequately dispersed particles. In Fig. 5b, with Au₈₅Ni₁₅, the color and shape were more uniform than the other two samples. In the whole area of the TEM, there was only one phase observed for thenanoparticles, in agreement with XRD results.

To confirm the core–shell structure of Au@Ni, we did a special elemental mapping of Au and Ni. Before the mapping, in order to be able to analyze the core of particles, we use HCl 1 M to etch the powder to reveal some of the cores of the particles. In Fig. 5(d), the red color is the response of gold and blue color is the nickel, suggesting AuNi bimetal shared one outmost layer of Au. This is important because the electro-oxidation rates depended strictly on the actual chemical and physical status of the redox mediator, which is influenced greatly by the morphological and compositional aspects of electrode outmost layers. A good physical dispersion of the catalytic centers leads to a highly active property towards ORR.

In order to verify this, the Au–Ni samples were heat-treated in Ar-H₂ at 750 °C for 72 h and cooled down again. There were neither new peaks nor changes of the position of the peaks. Fig. 6 showed the comparison of the Au₈₅Ni₁₅ XRD before and after 72 h of heat-treatment. Only the particles size became bigger calculated by

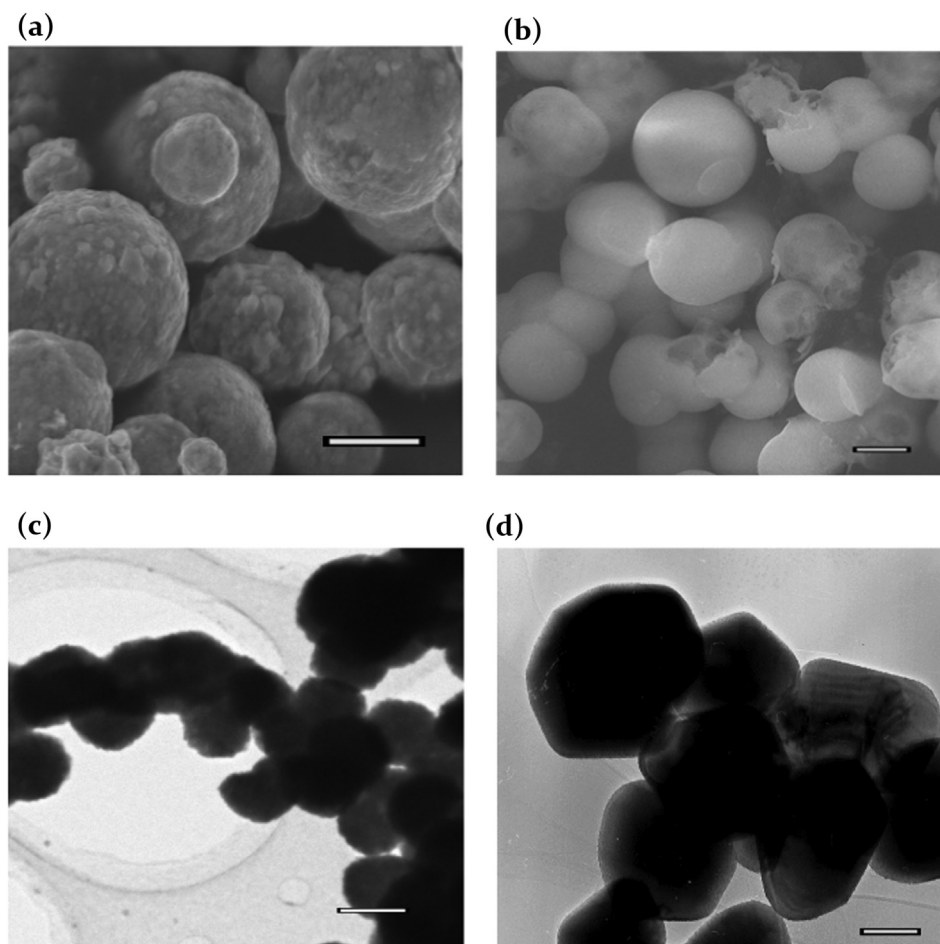


Fig. 7. SEM and TEM images of Au₈₅Ni₁₅ before and after 72 h of heat-treatment. (a) SEM before heat-treatment. (b) SEM after heat-treatment. (c) TEM before heat-treatment. (d) TEM after heat-treatment. The bar is 100 nm in (a) and (b), 10 nm in (c) and (d).

Scherrer's equation on the peak widths at half-maximum height of the sample. To observe the evolution of the particles after heat-treatment in the Ar–H₂, another SEM and TEM characterization of the Au₈₅Ni₁₅ sample were performed.

The SEM characterization shows that the morphology was much less uniform and a dramatically high amount of nanospheres were broken and conglomerated with each other (Fig. 7a and b). And the surface clumps evolved into facets, a totally different morphology. The SEM characterization shows that the particle size increased, too (Fig. 7c and d).

In the AuNi system, although evidence of the mode of Zener relaxation was reported and an intermediate decomposed state was found [20,21], it was difficult to conclude if the outmost layer was a meta-stable ordered phase or an intermediate state towards further evolution.

3.4. XPS analysis of the surface state of Au–Ni atoms

In order to understand the difference in the chemical oxidation states of the surface atoms, also to get the detailed species of the outmost layer of the nanoparticles, the XPS spectra of the Au and Ni elements were tested. All the binding energies were corrected by the principal peak's signal of the carbonaceous matrix using 284.8 eV as an internal standard. After that, the spectra were analyzed using XPSPEAK 4.1 software. And the spectra of the Au(4f) and Ni(2p) core level peaks of the samples after heat-treatment are presented in Fig. 8.

The XPS results of the Au₈₅Ni₁₅ demonstrated that the Au 4f^{7/2} peak was at 84.04 eV, compared to 83.73 eV for pure Au nanoparticles (Fig. 8a). The noble metal 4f peaks are known to shift to

higher energies upon forming bonds with other metals. [22] The result is in agreement with that conclusion. The Au 4f^{7/2} peaks of the Au₉₀Ni₁₀ and Au₇₅Ni₂₅ were also shifted to 84.00 eV and 84.10 eV (Fig. 8b), respectively. The more the Ni proportion was the stronger the shift was.

Caused by the multiplet splitting and shake up, the Ni spectra showed strong peaks in the higher binding energy side of the main peaks of 2p^{1/2} and 2p^{3/2}, the two pairs of peaks were typical of the transitional metal Ni. The Ni 2p^{3/2} peak at 852.46 eV in spectra Fig. 8c could only be attributed to the peak of Ni(0). But the binding energy shifted 0.26 eV compared with the binding energy of standard Ni(0) metal at 852.2 eV. Such a pronounced binding energy shift suggested that the electronic density of Ni and Au were greatly influenced by each other in this component, which resulted from the electronic interactions between Au and Ni atoms in the bimetal. After carefully analyzing the 2p peaks of Ni elements, it was found that there were no prominent differences in the Ni 2p^{3/2} peaks between all the samples, which meant the influences of Au on Ni atoms was not as strong as the influence of that Ni on Au atoms.

However, no AuO_x, Au(OH)_x, NiO_x or Ni(OH)_x species were observed in both cases. The chemical shift caused by the change of the surface electronic character of Au resulted in a synergistic activity between Au and Ni, affecting O–O splitting and enhancing the catalytic activity of ORR.

4. Electrochemical properties of the AuNi bimetals

In order to test the electrochemical impedance of the bimetal, AuNi powders were brush-painted with lab-fabricated solution on

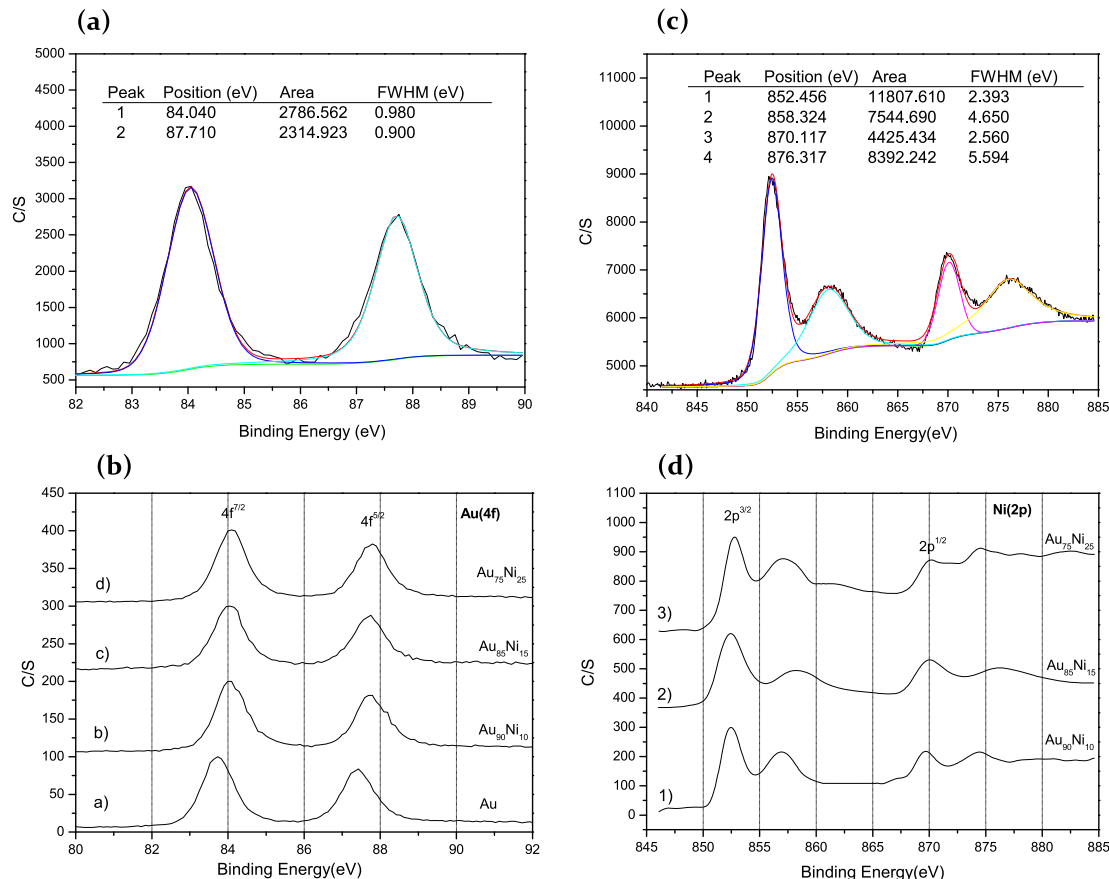


Fig. 8. XPS of Au(4f) and Ni(2p) of the samples. (a) XPS of Au(4f) of Au₈₅Ni₁₅. (b) XPS of Au(4f) of all samples. (c) XPS of Ni(2p) of Au₈₅Ni₁₅. (d) XPS of Ni(2p) of all samples.

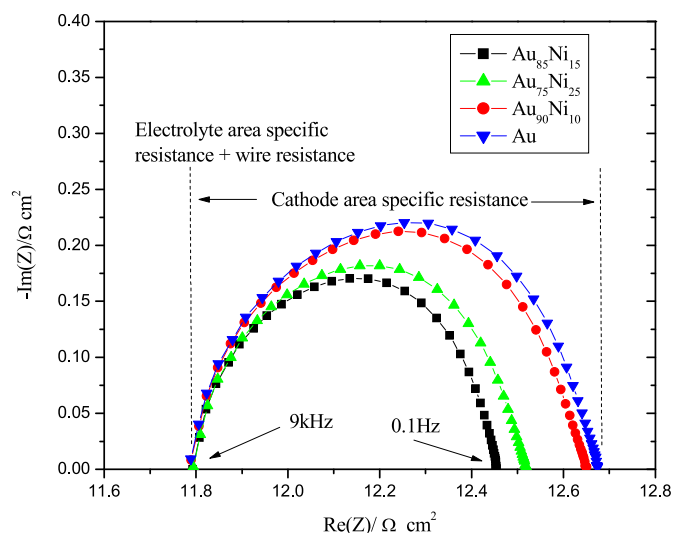


Fig. 9. Electrochemical impedance spectra of the half cells in O₂ at 500 °C.

each side of GDC electrolyte support symmetrically. The content of lab-fabricated solution is 0.40 g AuNi powder, 3 mL absolute ethyl alcohol, and 0.033 g Polyvinylpyrrolidone (PVP30) as thickener. Then they were evenly mixed in a mortar and painted to the surface of the electrolyte using a proper brush. After, it was and then fired at 750 °C for 2 h.

Each GDC support was polished to a thickness of 1.5 mm before being used. Fig. 9 showed the typical impedance spectrum of the half-cell containing the cathode-electrolyte interface measured and calculated at 500 °C. The resistance between the two intercepts with the real axis correspondent to the area-specific resistance (ASR) of the cathode-electrolyte interface. [23] The first intercept with the X axis was the electrolyte ASR plus the wire resistance. The theoretical electrolyte ASR of GDC with a thickness of 1.5 mm at 500 °C is 11.6 Ω cm² [24].

The experimentally measured electrolyte ASR plus the wire resistance, for the Au, Au₉₀Ni₁₀, Au₈₅Ni₁₅ and Au₇₅Ni₂₅ samples, were 11.79, 11.78, 11.79 and 11.78 Ω cm² respectively, were in

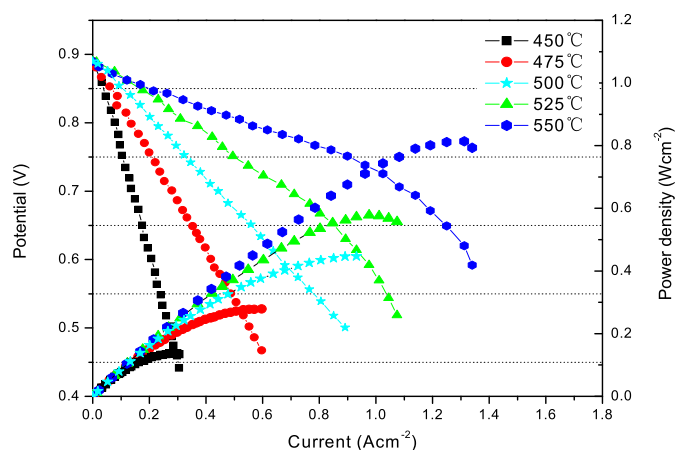


Fig. 11. I–V curves and the corresponding power densities at 450, 475, 500, 525, 550 °C.

agreement with that value, providing evidence that the electrochemical impedance spectrum was an actual reflection of the cell. The ASR value of the cathode-electrolyte interface for Au, Au₉₀Ni₁₀, Au₈₅Ni₁₅ and Au₇₅Ni₂₅ were 0.89, 0.87, 0.66, and 0.72 Ω cm², respectively. Practically, bimetallic catalysts exposed to the reaction medium, in this case, O₂, were surface AuNi bimetal or mixture type with both metals. However, preferential surface segregation of one metal occurred as mentioned above. The surface energies of Ni were bigger but the specific gravity of which was smaller, which would cause a competition of preferential surface segregation between the Au and Ni elements. It was noticed when the bulk composition of Au:Ni was 85:15, the dynamic equilibrium of the surface elements reached their best catalytic point, hence processing the smallest impedance. Fig. 10 shows the corresponding Arrhenius plots log(ASR) = f(1000/T) for the half cells in O₂ at 450, 475, 500, 525, 550 °C. The calculated E_a for Au, Au₉₀Ni₁₀, Au₈₅Ni₁₅ and Au₇₅Ni₂₅ samples as a function of the temperature was 2.42, 2.40, 2.31 and 2.36 eV, respectively. In the thermally activated process of ORR, there were no huge differences of E_a for the four samples. A similar behavior was highlighted. And the evolution of the log(ASR) was linear and there was no change of slope for temperature between 450 and 550 °C. The E_a of Au₈₅Ni₁₅ was the lowest amongst all the samples.

Fig. 11 shows the current–voltage relationships and the calculated power densities of the single fuel cell using Au₈₅Ni₁₅ as the cathode. The data were recorded after the fuel cell stabilized for 60 min. The Open Circuit Voltage of the fuel cell was 0.89 V. The acquired highest power densities were 133, 279, 440, 575, and 810 mW cm^{−2} at 450, 475, 500, 525, 550 °C, respectively. However, when the current was above 1 A cm^{−2}, the concentration polarization of the cell became severe. The results of the other samples were also listed in Table 1.

Fig. 12 shows the polished cross-sectional microstructure and the magnified interface for cathode and electrolyte. The thickness

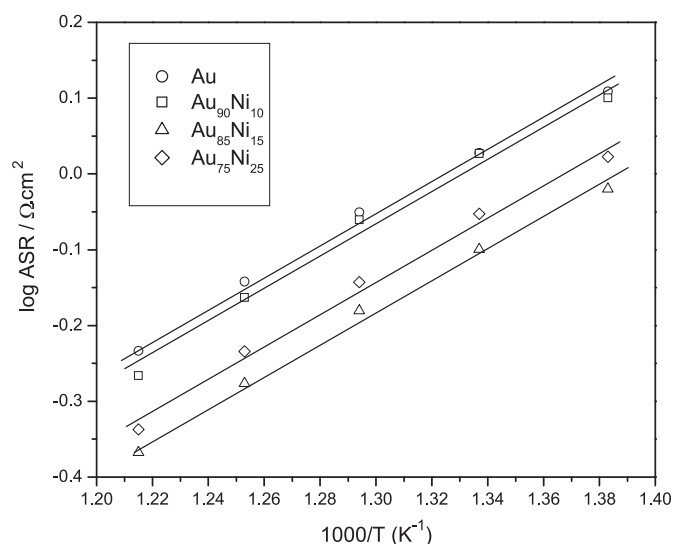


Fig. 10. Corresponding Arrhenius plots for the half cells in O₂ at 450, 475, 500, 525, 550 °C.

Table 1

The d_{111} value, Au4f^{7/2} peak, Ni2p^{3/2} peak, ASR and maximum power output.

	Au ₉₀ Ni ₁₀	Au ₈₅ Ni ₁₅	Au ₇₅ Ni ₂₅	Au
Au d_{111} value	0.232 nm	0.232 nm	0.230 nm	0.236 nm
Au 4f ^{7/2}	84.00 eV	84.04 eV	84.10 eV	83.73 eV
Ni 2p ^{3/2}	852.46 eV	852.46 eV	852.70 eV	N/A
ASR (500 °C)	0.87 Ω cm ²	0.66 Ω cm ²	0.72 Ω cm ²	0.89 Ω cm ²
Max. Output (500 °C)	374 mW cm ^{−2}	440 mW cm ^{−2}	398 mW cm ^{−2}	0.355 mW cm ^{−2}

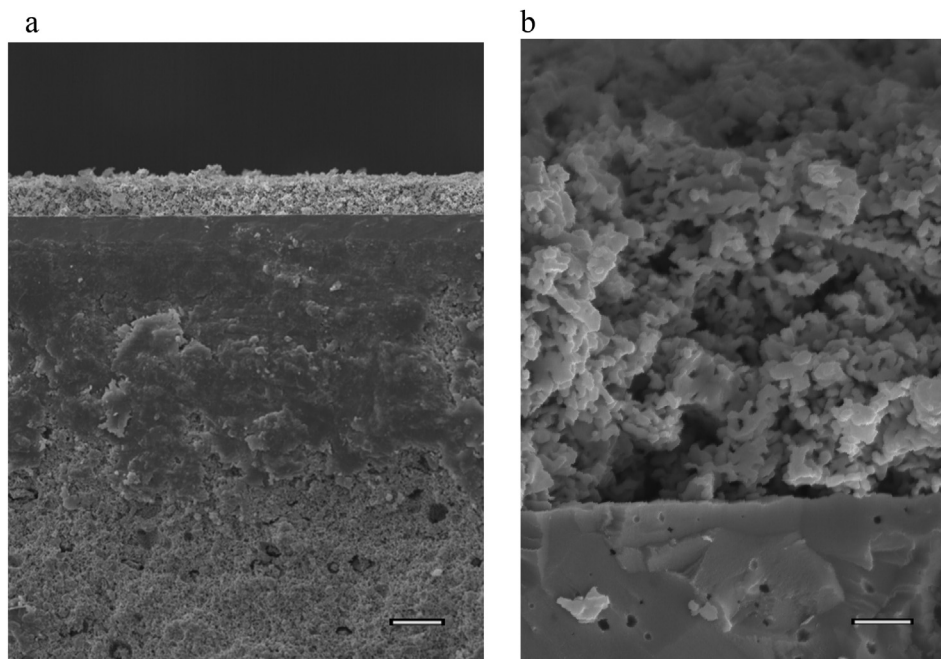


Fig. 12. Polished cross-sectional microstructure and the magnified interface for cathode and electrolyte. (a) cross-sectional microstructure (b) magnified interface of cathode and electrolyte. The bar is 10 μm in (a) and 1 μm in (b).

of the anode was about 0.8 mm, which supported the whole cell, shown in Fig. 12a. The electrolyte layer was about 25 μm , well densified by sintering as shown in Fig. 12b. After brush-painted onto the polished electrolyte and co-fired to adhere onto the surface, the AuNi particles formed an active cathode layer as thick as about 10 μm . It can clearly be observed from the SEM image that the cathode layer was evenly distributed, which was beneficial for the formation of the electronic conducting network within the cathode. The porous cathode due to the use of PVP permitted the infiltration of oxygen to the Three Phase Boundaries (TPBs). In addition, the amount of oxygen adsorbed on the metal/ceramic might also have been increased because of the pores. The oxygen reduction reaction, which mainly took place at the TPBs could therefore be accelerated. High performance is assured but the nanoparticles' long term stability still need to be further considered.

5. Conclusions

It is possible to synthesize the Au–Ni bimetal by taking advantage of the phase separation mechanism in aqueous solutions and post heat-treatment. The bulk composition of Au–Ni was calculated to be $\text{Au}_{90}\text{Ni}_{10}$, $\text{Au}_{85}\text{Ni}_{15}$ and $\text{Au}_{75}\text{Ni}_{25}$ indexed by ICP-AES and the valence of surface Au and Ni was proved by X-ray photoelectron spectroscopy (XPS) to be Au(0), Ni(0). Partially substitution of Au by Ni benefited the catalytic activity towards the ORR while saving 25% of noble metal. Taking advantages of this phase separation mechanism of the AuNi system was the key in the experimental studies. Also, the electrochemical experiments indicated some synergistic interaction between the gold and nickel species towards the electrocatalytic ORR. The maximum power density generated is 810 mW cm^{-2} at 550 $^{\circ}\text{C}$, with the $\text{Au}_{85}\text{Ni}_{15}$ powder as cathode.

Acknowledgment

The authors acknowledge the Portuguese Foundation for Science and Technology (FCT) for financial support via the SFRH/BPD/86336/2012.

References

- [1] F. Abraham, M.F. Debreuille-Gresse, G. Mairese, G. Nowogrochi, *Solid State Ionics* 28–30 (1988) 529–532.
- [2] B.C.H. Steele, *Solid State Ionics* 129 (2000) 95–110.
- [3] J.B. Goodenough, A. Manthiram, M. Paranthaman, Y.S. Zhen, *Mater. Sci. Eng. B* 12 (1992) 357–364.
- [4] C.R. Xia, M.L. Liu, *Solid State Ionics* 144 (2001) 249–255.
- [5] E.P. Murray, S.A. Barnett, *Solid State Ionics* 143 (2001) 265–273.
- [6] R.W. Reeve, P.A. Christensen, A. Hamnett, S.A. Haydock, S.C. Roy, *J. Electrochem. Soc.* 145 (1998) 3463–3471.
- [7] N.A. Vante, H. Tributsch, *Nature* 323 (1986) 431–432.
- [8] J. Prakash, D.A. Tryk, W. Aldred, E.B. Yeager, *J. Appl. Electrochem.* 29 (1999) 1463–1469.
- [9] S.L. Gojkovic, S. Gupta, R.F. Savinell, *J. Electroanal. Chem.* 462 (1999) 63–72.
- [10] J. Fournier, G. Lalande, R. Cote, *J. Electrochem. Soc.* 144 (1997) 218–226.
- [11] G. Chen, D.G. Xia, Z.R. Nie, Z.Y. Wang, L. Wang, L. Zhang, J.J. Zhang, *Chem. Mater.* 19 (2007) 1840–1844.
- [12] D.G. Xia, G. Chen, Z.Y. Wang, J.J. Zhang, S.Q. Hui, D. Ghosh, H.J. Wang, *Chem. Mater.* 18 (2006) 5746–5749.
- [13] T. Yang, L.J. Zhang, X. Li, D.G. Xia, *J. Alloys Compd.* 492 (2010) 83–87.
- [14] J.H. Sinfelt, *Bimetallic Catalysts: Discoveries, Concepts and Applications*, Wiley, New York, 1983.
- [15] Y. Yato, M. Kajihara, *Mater. Sci. Eng. A* 428 (2006) 276–283.
- [16] T. Yang, F. Li, D.G. Xia, *J. Power Sources* 195 (2010) 2514–2519.
- [17] G.C. Bond, D.T. Thompson, *Gold Bull.* 33 (2000) 41–51.
- [18] G.C. Bond, D.T. Thompson, *Catal. Rev. Sci. Eng.* 41 (1999) 319–388.
- [19] G.J. Hutchings, M. Haruta, *Appl. Catal. A* 291 (2005) 2–5.
- [20] Y. Hu, Y.V. Tolmachev, D.A. Scherson, *J. Electroanal. Chem.* 468 (1999) 64–69.
- [21] R. Brayner, T. Coradin, M.J. Vaulay, C. Mangeney, J. Livage, F. Fiévet, *Colloids Surf. A* 256 (2005) 191–197.
- [22] G.C. Wang, J. Jiao, X.H. Bu, *J. Phys. Chem. C* 111 (2007) 12335–12339.
- [23] Z.P. Shao, S.M. Halle, *Nature* 431 (2004) 170–173.
- [24] H. Inaba, H. Tagawa, *Solid State Ionics* 83 (1996) 1–16.